THE JOURNAL OF PHYSICAL CHEMISTRY C
A JOURNAL OF THE AMERICAN CHEMICAL SOCIETY

pubs.acs.org/JPCC

Article

Calcium Cosalt Addition to Alter the Cation Solvation Structure and Enhance the Ca Metal Anode Performance

Alan T. Landers, Julian Self, Scott A. McClary, Keith J. Fritzsching, Kristin A. Persson, Nathan T. Hahn, and Kevin R. Zavadil*

Cite This: J. Phys. Chem. C 2023, 127, 23664−23674

Read Online

ACCESS | Metrics & More | Article Recommendations | Supporting Information

ABSTRACT: Accessing the energy density and sustainability of calcium metal batteries requires mastering reversible calcium electrodeposition through electrolyte design. Several electrolytes support reversible, ambient temperature deposition but at utilization and rate too low for practical applications. These challenges stem from solvation structures characterized by either high barriers for cation desolvation or thermodynamic instability, leading to parasitic decomposition of the salt and solvent. The optimal solvation structure for the effective delivery of calcium to the electrode interface is not known. In this work, we show that adding a relatively small amount of a weakly associating calcium salt (calcium carba-*closo*-dodecaborate) to an otherwise strongly associated solution (calcium borohydride in tetrahydrofuran) produces a surprising population of fully solvent-coordinated Ca^{2+} cations in the form of solvent-separated ion pairs (SSIPs). We further demonstrate that the formation of these SSIPs beneficially impacts the kinetics and thermodynamics of calcium electrodeposition, revealing the unexpected finding that direct coordination of Ca^{2+} by the BH_4^- anion limits the electrodeposition process. These findings reveal how the competition between solvent and anion coordination to Ca^{2+} affects calcium deposition kinetics and cycling stability, setting the stage for a new calcium electrolyte design based on mixed anion electrolytes.

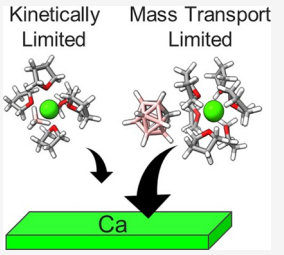

INTRODUCTION

To meet society's growing needs for renewable energy storage, novel battery chemistries with higher energy density and lower cost than Li-ion batteries need to be developed.[1,2] Ca metal batteries have been proposed as alternatives to Li-ion batteries due to the greater crustal abundance (41,500 mg/kg for Ca vs 20 mg/kg for Li)[3] and anode capacity (1337 mAh/g for Ca metal anodes vs 372 mAh/g for Li/C_6 anodes). Despite these advantages, development of Ca metal batteries has been limited.[2,4−13]

Relatively few Ca^{2+} electrolytes are capable of reversible Ca plating and stripping due to the reactivity of Ca^{2+} electrolytes with the metal anode. The first successful demonstrations utilized $Ca(BF_4)_2$/ethylene carbonate/propylene carbonate electrolytes and required temperatures of 75 °C or greater while displaying relatively low efficiencies.[14] A later work demonstrated reversible plating and stripping from this electrolyte at room temperature, albeit at low current densities (<1 mA/cm^2).[15] Furthermore, significant F content was observed in the deposits, indicating the degradation of the $Ca(BF_4)_2$ salt.[14,15] Reversible plating and stripping of Ca at room temperature and current densities greater than 1 mA/cm^2 were first demonstrated using $Ca(BH_4)_2$/tetrahydrofuran (THF) electrolytes.[16] Coulombic efficiencies (CE) as high as 97% have been reported using this electrolyte.[17−19] More recently, electrolytes using calcium salts with weakly coordinating anions (WCAs) have been developed with the goal of widening the electrochemical stability window of the electrolyte. Two groups concurrently reported the synthesis and testing of calcium tetrakis(hexafluoroisopropoxy) borate ($Ca(BHFIP)_2$)/dimethoxyethane (DME) electrolytes with CE as high as 92%.[20,21] As with $Ca(BF_4)_2$/EC/PC, deposits from this electrolyte displayed significant F content, indicating salt decomposition.[20,21] Similarly, calcium tetrakis-(hexafluoroisopropoxy) aluminate ($Ca(AlHFIP)_2$) /DME and calcium tetrakis(perfluoro-*tert*-butoxy) aluminate ($Ca(TPFA)_2$) /DME electrolytes exhibit instability at Ca deposition potentials.[8,22] Furthermore, despite magnesium bis(trifluoromethylsulfonyl)imide ($MgTFSI_2$) being used to successfully cycle Mg metal,[23,24] $CaTFSI_2$ has been shown to be incapable of reversibly plating and stripping Ca metal in ethereal electrolytes, likely due to the decomposition of the $TFSI^-$ anion.[25] As an alternate class of WCA electrolytes lacking F, calcium carba-*closo*-dodecaborate ($Ca(CB_{11}H_{12})_2$) /DME/THF displayed reversible calcium plating and stripping with CE as high as 88%.[26] While these efforts have proven that reversible Ca plating and stripping are possible, the rational design of electrolytes will require connecting the speciation of the Ca-ion electrolyte to its ability to reversibly cycle Ca metal.

Received: August 25, 2023
Revised: November 14, 2023
Accepted: November 15, 2023
Published: December 4, 2023

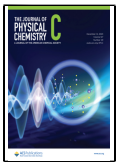

https://doi.org/10.1021/acs.jpcc.3c05757
J. Phys. Chem. C 2023, 127, 23664−23674

Of these electrolytes, the speciation of $Ca(BH_4)_2$/THF has been most thoroughly investigated. A comparison of $Ca(BH_4)_2$/THF and $Mg(BH_4)_2$/THF electrolytes found that the larger size and greater polarizability of the Ca^{2+} cation allow for greater configurational flexibility, enabling the formation of complexes such as the neutral monomer $Ca(BH_4)_2$, neutral dimer $Ca_2(BH_4)_4$, and ionic clusters such as $CaBH_4^+$ and $Ca(BH_4)_3^-$.[17] The concentrations of these species were later elucidated using a combination of pulsed-field-gradient nuclear magnetic resonance (PFG-NMR) and dielectric relaxation spectroscopy (DRS).[27] These studies revealed that the concentration of the $CaBH_4^+$ contact ion pair (CIP), which was proposed to be the active species for calcium plating and stripping,[17] remains below 0.1 M even at $Ca(BH_4)_2$ concentrations of 1.5 M.[27] Recent computational advances confirm this critical role of the CIP and indicates that its interfacial concentration might be enhanced relative to the bulk at cathodic potentials.[28] Furthermore, the analysis of ultramicroelectrode voltammetry in $Ca(BH_4)_2$/THF identified a chemical−electrochemical mechanism, with the chemical step limiting Ca deposition.[18] These findings suggest that the calcium deposition rate could be improved by increasing the concentration of the $CaBH_4^+$ contact ion pair or by tailoring the identity of the reactive Ca complex to avoid the limiting chemical step during deposition.

The ideal Ca-ion electrolyte must allow for both the close approach of the Ca-ion complex to the reactive interface and enable facile electron transfer at the interface. Recent molecular dynamic free-energy sampling simulations have identified that the presence of anions in the first solvation shell enables Mg and Li complexes to approach a negatively charged interface more closely than complexes with only the solvent in the first shell.[29,30] Additionally, we know that anion participation in the first solvation shell can contribute to anion decomposition with electron transfer.[31] A key factor in probing the kinetic effects of desolvation is the selection of anions with extraordinary reductive stability, including $CB_{11}H_{12}^-$ and BH_4^- to minimize such competing thermodynamic effects.[16,32] While a close approach of the Ca complex to the reactive interface is necessary for electron transfer, the likelihood of charge transfer still depends on its mechanism and the structure of the cation solvation complex. The association strength of anions to multivalent Mg^{2+} and Zn^{2+} ions has been shown to alter the overpotential for metal plating and stripping, with more weakly associated anions correlated to lower overpotentials for metal deposition and greater overpotentials for metal stripping.[33] These results demonstrate that coordination can shift the tendency for electron transfer to a reactive complex. Thus, we aim to design electrolytes with Ca species that include partial anion coordination to allow for a close approach to the reactive interface while maintaining facile charge transfer to the complex.

In this work, we explore the relationship between electrolyte speciation as a function of anion coordination strength and electrochemical performance in aprotic calcium electrolytes. We hypothesize that the addition of a weakly coordinating Ca salt to $Ca(BH_4)_2$/THF electrolytes should increase the concentration of the $CaBH_4^+$ CIP, the previously proposed complex for Ca^{2+} delivery to the electrode interface,[17] thereby enhancing the CE and increasing the current density at which the electrolyte can be cycled. While the presence of $Ca(BH_4)_2$ limits the electrolyte's oxidative (hydride oxidation) and reductive (hydrogen production) stability, the well-characterized speciation of $Ca(BH_4)_2$/THF electrolytes makes it an ideal candidate for manipulating electrolyte speciation.[27] Previous attempts to add weakly coordinating Ca salts to $Ca(BH_4)_2$/THF electrolytes, utilizing $Ca(TFSI)_2$ as a weakly coordinating Ca salt, were limited by complex speciation in these electrolytes as well as reductive decomposition of the $TFSI^-$ anion, limiting Ca stripping.[34,35] We propose that $Ca(CB_{11}H_{12})_2$ could serve as a more ideal weakly coordinating salt due to the weaker coordination of $CB_{11}H_{12}^-$ to Ca^{2+} and its demonstrated ability to plate and strip Ca metal in ethereal solvents.[26] Through the combination of ionic conductivity, Raman spectroscopy, nuclear magnetic resonance (NMR) spectroscopy, and DRS, we determine that the addition of $Ca(CB_{11}H_{12})_2$ unexpectedly produces $Ca(CB_{11}H_{12})^+$ solvent-separated ion pairs (SSIP). We then used cyclic voltammetry (CV) and galvanostatic cycling to elucidate the effect of altered speciation on the electrochemical behavior. This work provides insights into the design of a more efficient coordination complex for delivering a multivalent ion to an electrode interface, demonstrating that the removal of a strongly bound anion from the first solvation shell favors charge transfer to the complex.

METHODS

Electrolyte Preparation. Before use, commercially purchased $Ca(BH_4)_2$·2THF was dried under vacuum at 190 °C for 4 h to remove THF, and $NaBH_4$ was dried under vacuum at 130 °C for 3 h. THF was vacuum-distilled over metallic sodium before storage with activated alumina and molecular sieves. Typical water concentrations in THF were measured to be 1−2 ppm using Karl Fischer titration. $NaBH_4$−THF stock solutions (∼12 mM) were prepared following previously reported methods.[19] As demonstrated in our previous work, sodium is a contaminant in commercially supplied $Ca(BH_4)_2$·2THF. Sodium concentration varies among lot number, and dilute $NaBH_4$ concentrations were previously found to be necessary to obtain dense Ca deposits from $Ca(BH_4)_2$/THF electrolytes.[19]

$Ca(CB_{11}H_{12})_2$ was synthesized inside a glovebox. Approximately 5 mmol (∼1 g) of $TMAHCB_{11}H_{12}$ (Katchem spol. s r.o.) was dissolved in 5 mL of THF. In a separate vial, approximately 2.5 mmol (∼0.174 g) of dried $Ca(BH_4)_2$ was dissolved in 5 mL of THF. The $Ca(BH_4)_2$ solution was stirred on a hot plate at room temperature. The $TMAHCB_{11}H_{12}$ solution was added to the $Ca(BH_4)_2$ solution, dropwise, in 500 uL aliquots. Approximately 1 min elapsed between each aliquot to allow bubbling to subside. During the addition, a white powder began to form. After the last aliquot was added, the solution was allowed to stir for 30−60 min at room temperature. The hot plate was then heated to 45 °C, and the solution was stirred overnight. The solvate powder was collected by using vacuum filtration. The powder was thoroughly washed using distilled THF by both direct washing and resuspension of the powder in THF, followed by vacuum filtration for a total of three wash cycles. The powder was then dried overnight on a Schlenk line at 60 °C before being returned to the glovebox. The powder purity was checked using ^1H and ^{11}B NMR.

Mixed-salt electrolytes were prepared by first adding appropriate amounts of dried $Ca(BH_4)_2$ and $Ca(CB_{11}H_{12})_2$ to a vial. Neat THF and the $NaBH_4$-THF solution were added to the vial to achieve the desired concentrations of $Ca(BH_4)_2$, $Ca(CB_{11}H_{12})_2$, and $NaBH_4$ (∼4 mM).[19] Electrolytes were

https://doi.org/10.1021/acs.jpcc.3c05757
J. Phys. Chem. C 2023, 127, 23664−23674

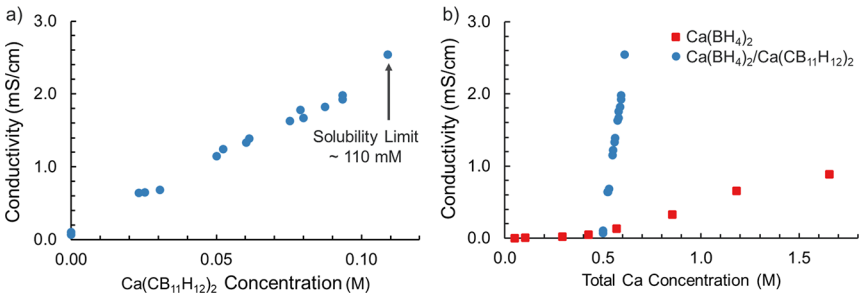

Figure 1. (a) Ionic conductivity of 500 mM $Ca(BH_4)_2$/y mM $Ca(CB_{11}H_{12})_2$/THF electrolytes. (b) Comparison of the ionic conductivity between $Ca(BH_4)_2$/THF and $Ca(BH_4)_2/Ca(CB_{11}H_{12})_2$/THF electrolytes. The $Ca(BH_4)_2$/THF electrolyte conductivity data in (b) was taken from ref 17. Copyright 2020 Royal Society of Chemistry.

stirred for at least 16 h prior to use to ensure equilibration of the electrolyte prior to electrochemical and characterization experiments.

Conductivity Measurements. Ionic conductivity of the electrolytes was measured using potentiostatic electrochemical impedance spectroscopy over a frequency range from 1 to 100 kHz with a custom conductivity probe consisting of two parallel Pt electrodes. The probe was calibrated regularly using 1 and 10 mM aqueous KCl solutions with an average cell factor of 0.83 cm^{-1} determined for the measurements in this work.

Raman Measurements. Raman spectroscopy measurements were made using a Horiba T64000 instrument with a 458 nm laser, Synapse/Symphony II detector, and a diffraction grating system with 1800 gr/mm. Twenty scans were collected with an acquisition time of 10 s per point except at the highest concentration of $Ca(CB_{11}H_{12})_2$ where the acquisition was collected at 5 s per point to prevent detector saturation. The measurements were collected over a range of 450−3650 cm^{-1}.

^{43}Ca NMR Measurements. ^{43}Ca NMR measurements were collected by using a Bruker NMR spectrometer at a resonant frequency of 500 MHz. The low natural abundance of the ^{43}Ca isotope as well as its low gyromagnetic ratio requires long acquisition times (∼14 h) to achieve acceptable signal/noise ratios. Low-temperature experiments were conducted using an external chiller which enabled experiments at temperatures as low as 255 K.

DRS Measurements. DRS measurements were performed over a frequency range from 0.5 to 26.5 GHz by using a Keysight N1501A dielectric probe kit with a Keysight 9375A vector network analyzer. The measurements were calibrated using air, water, and THF. The real and imaginary components of the measured permittivity were fit simultaneously using three Debye relaxations, following previous DRS analysis of $Ca(BH_4)_2$/THF electrolytes.[27] For fitting, the ionic conductivity of the electrolytes was fixed at the experimentally measured values. For higher conductivity samples (53 and 81 mM added $Ca(CB_{11}H_{12})_2$), the data for ε'' were fit over 0.7−26.5 GHz to avoid unphysical responses.[36] The parameters determined from fitting the data are reported in Table S1.

To calculate the dielectric increments, density functional theory (DFT) was used to optimize the structures and recover the dipole moments, which were then used to estimate the dielectric increments. Quantum chemistry (DFT) calculations were completed with Gaussian 16.[37] The basis set used was 6-31+g(d,p) with the wb97xd functional.[38] Dipole moment calculations were carried out with a continuum solvation model.[39] Specifically, the polarizable continuum model was used[40] with the dielectric constant set to 7.4, that of the neat THF solvent. Via DFT, the first solvation shell of the calcium ions was explicitly treated. To deconvolute the dielectric spectra features, we optimize the structures for $Ca(CB_{11}H_{12})^+$ SSIP species (6THF-Ca^{2+}-$CB_{11}H_{12}^-$ and 5THF-Ca^{2+}-BH_4^--$CB_{11}H_{12}^-$) using DFT. The calculated dipole moments were 35.5 and 34 D for 6THF-Ca^{2+}-$CB_{11}H_{12}^-$ and 5THF-Ca^{2+}-BH_4^--$CB_{11}H_{12}^-$, respectively. Using the Cavell equation (eq 1) and assuming negligible correlations beyond the first solvation shell, we calculate a dielectric increment[41,42]

$$\Delta\varepsilon_i = \frac{3\varepsilon}{2\varepsilon + 1}\frac{\mu^2_{\text{solution}}}{3k_B T\varepsilon_0} \quad (1)$$

We calculate the net dielectric increment by subtracting a fixed value from the gross dielectric increment to account for the binding of the THF molecules in the SSIP structures. For 6THF-Ca^{2+}-$CB_{11}H_{12}^-$, we subtract a value of 8.8 M^{-1}, as determined in previous work.[36] For 5THF-Ca^{2+}-BH_4^--$CB_{11}H_{12}^-$, we subtract a value of 7.3 M^{-1}.

Electrochemical Measurements. Electrochemical measurements were performed in an Ar-filled glovebox. Measurements were conducted in a glass T-cell using a Solartron ModuLab XM potentiostat. The working electrodes were 1.6 mm diameter Au electrodes mounted in a nonconductive shroud. These electrodes were first soaked in 1 M HCl, followed by mechanical polishing with 50 nm diameter alumina to remove residual Ca. The Au electrodes were dried in a vacuum oven overnight prior to use. The counter and reference electrodes consisted of freshly abraded Ca rods. The working electrode and counter electrode faced each other with a typical gap of 2−5 mm. *iR* correction was performed by first measuring the uncompensated resistance (R_u) of the cell at the open circuit using potentiostatic electrochemical impedance spectroscopy. The potentiostat was then set to compensate for the measured resistance in situ during cyclic voltammetry. For the 500 mM $Ca(BH_4)_2$/THF electrolyte, the measured R_u exceeded the value which can be compensated by the potentiostat in situ. Therefore, the potentiostat was used to correct for 10,000 Ω of R_u in situ, and the remaining R_u was compensated mathematically after data collection. The second CV cycle is shown in this work due to alloying/dealloying effects observed in the first CV cycle using these electrolytes.[19]

Cycling experiments were conducted in the same T-cell configuration with Ca counter and reference electrodes. Average Coulombic efficiency was determined using a Cal|Au cell by repeatedly depositing and stripping 0.5 mAh/cm^2 Ca on Au over a range of current densities for five cycles. Longer term cycling stability was evaluated using a Cal|Ca cell where Au was replaced with a freshly polished Ca rod as the working

https://doi.org/10.1021/acs.jpcc.3c05757
J. Phys. Chem. C 2023, 127, 23664−23674

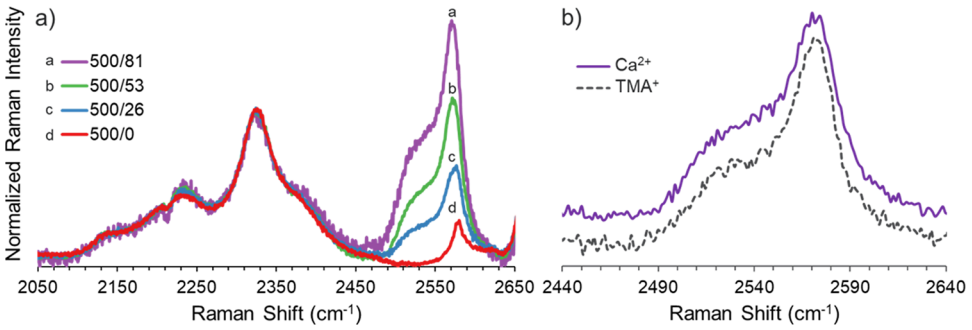

Figure 2. (a) Variation in Raman ν(B−H) spectra of 500 mM $Ca(BH_4)_2$/THF with the addition of $Ca(CB_{11}H_{12})_2$. Data labels are abbreviated as x mM $Ca(BH_4)_2$/y mM $Ca(CB_{11}H_{12})_2$. (b) Comparison of the collective ν(B−H) mode for the $CB_{11}H_{12}$ anion as a 500/75 mixture for the Ca^{2+} salt vs the 75 mM $TMAH^+$ salt in THF.

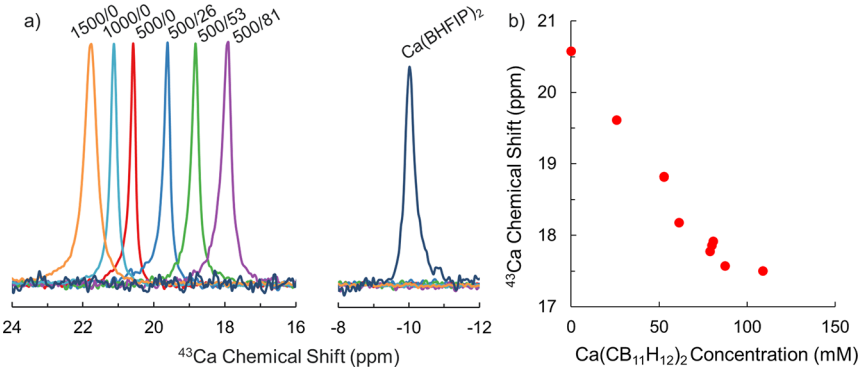

Figure 3. (a) Measured ^{43}Ca NMR spectra for $Ca(BH_4)_2$/$Ca(CB_{11}H_{12})_2$/THF and 400 mM $Ca(BHFIP)_2$/THF electrolytes. Data labels are abbreviated as x mM $Ca(BH_4)_2$/y mM $Ca(CB_{11}H_{12})_2$. (b) ^{43}Ca chemical shift as a function of $Ca(CB_{11}H_{12})_2$ added to 500 mM $Ca(BH_4)_2$/THF electrolytes.

electrode. Cycling was conducted with 0.5 mAh/cm^2 calcium at 2 mA/cm^2 up to 50 h.

Reduction Potential Calculations. Gas-phase optimization of the structures was completed, and single-point corrections in the THF solution environment (modeled via an explicit solvation shell and the continuum solvation model) were undertaken for the solvation energies before reduction. During the reduction process (by one electron, as in Hou et al.[43]), it was assumed that one solvent molecule is lost from the first solvation shell. For this step, optimization was undertaken in solution phase, allowing the calculation of the one electron reduction potential. Calculations performed with no change in the solvation shell demonstrate similar trends in reduction potential (Table S2). It was verified that the charge transfer was to the calcium cation via natural bond order (NBO) charge analysis.

Scanning Electron Microscopy. Scanning electron microscopy (SEM) images were acquired by using an FEI Magellan 400 microscope. Samples were mounted on a sample stage in an Ar-filled glovebox and transferred under an inert atmosphere to the SEM system via an Ar-filled glovebag for analysis.

RESULTS AND DISCUSSION

Manipulating Electrolyte Speciation. We hypothesize that the addition of $Ca(CB_{11}H_{12})_2$ to $Ca(BH_4)_2$/THF electrolytes will increase the population of the $CaBH_4^+$ CIP, as shown in R1.

Table 1. Summary of Electrolyte Speciation and the Measured ^{43}Ca Chemical Shift

composition	speciation	^{43}Ca chemical shift
0.4 M $Ca(BH_4)_2$/0.4 M $LiBH_4$/THF	$Ca(BH_4)_2$−$LiBH_4$−THF clusters[46]	37.5[46]
1.5 M $Ca(BH_4)_2$/THF	35% $Ca(BH_4)_2$, 54% $Ca_2(BH_4)_4$, 5% $CaBH_4^+$, 5% $Ca(BH_4)_3^-$[27a]	21.8
1.0 M $Ca(BH_4)_2$/THF	40% $Ca(BH_4)_2$, 56% $Ca_2(BH_4)_4$, 2% $CaBH_4^+$, 2% $Ca(BH_4)_3^-$[27a]	21.1
0.5 M $Ca(BH_4)_2$/THF	52% $Ca(BH_4)_2$, 48% $Ca_2(BH_4)_4$, < 1% $CaBH_4^+$, < 1% $Ca(BH_4)_3^-$[27a]	20.6
0.5 M $Ca(BH_4)_2$/26 mM $Ca(CB_{11}H_{12})_2$/THF	see text	19.6
0.5 M $Ca(BH_4)_2$/53 mM $Ca(CB_{11}H_{12})_2$/THF	see text	18.8
0.5 M $Ca(BH_4)_2$/81 mM $Ca(CB_{11}H_{12})_2$/THF	see text	17.9
0.4 M $Ca(BHFIP)_2$/THF	90% Ca^{2+}, 10% $Ca(BHFIP)^+$ SSIP[36]	−10.0
0.5 M $Ca(TFSI)_2$/THF	mixture of neutral $Ca(TFSI)_2$ and $CaTFSI^+$ CIPs[47]	−19.1[47]
0.1 M $Ca(TFSI)_2$/THF	mixture of neutral $Ca(TFSI)_2$ and $CaTFSI^+$ CIPs[47]	−19.8[47]

[a]Percentage of Ca contained within the given complex.

$$Ca(BH_4)_2 + Ca(CB_{11}H_{12})_2 \rightleftharpoons 2CaBH_4^+ + 2CB_{11}H_{12}^- \quad \text{(R1)}$$

However, a single equilibrium does not adequately describe the speciation of the mixed-salt electrolyte. The single-salt $Ca(BH_4)_2$/THF electrolyte exists as a mixture of neutral

https://doi.org/10.1021/acs.jpcc.3c05757
J. Phys. Chem. C 2023, 127, 23664−23674

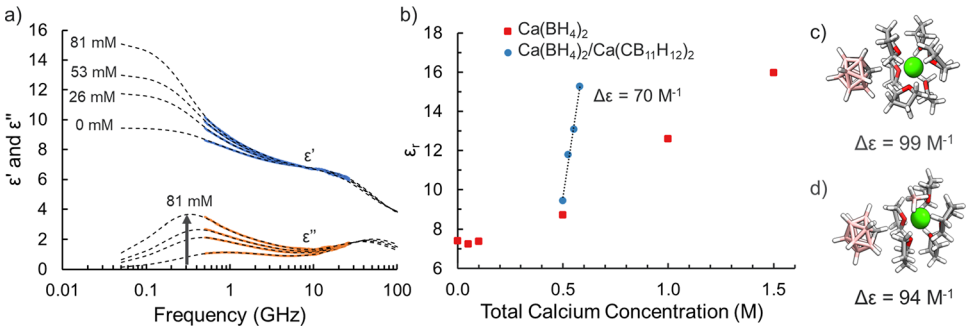

Figure 4. (a) Real (ε', blue) and imaginary (ε'', orange) components of the complex permittivity measured for 500 mM $Ca(BH_4)_2$/y mM $Ca(CB_{11}H_{12})_2$/THF electrolytes. Solid lines represent the measured data, while dashed lines represent the fits to these data. (b) Comparison of the total solution dielectric constants (ε_r) for $Ca(BH_4)_2$/THF and $Ca(BH_4)_2/Ca(CB_{11}H_{12})_2$/THF electrolytes extracted from the fits of the measured permittivity. The $Ca(BH_4)_2$/THF data are reproduced with permission from the American Chemical Society.[27] A linear fit of ε_r as a function of concentration for the $Ca(BH_4)_2/Ca(CB_{11}H_{12})_2$/THF electrolyte is shown as a dotted line. (c, d) Calculated net dielectric increment for $Ca(CB_{11}H_{12})^+$ SSIP and $CaBH_4(CB_{11}H_{12})$ SSIP.

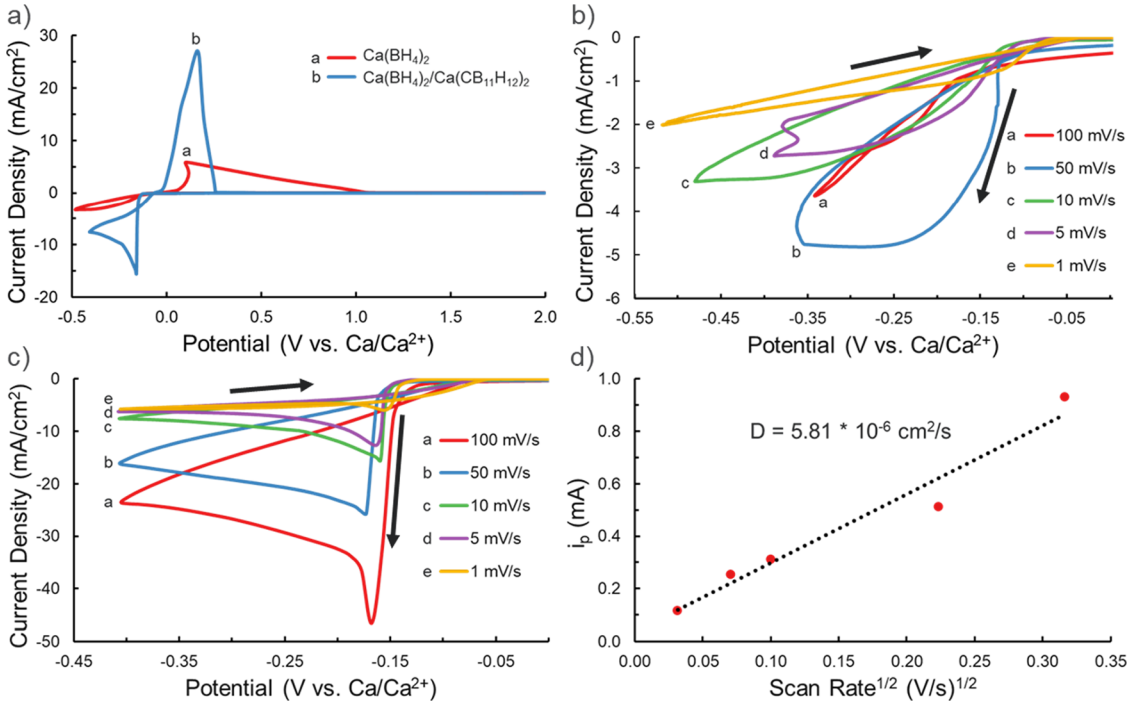

Figure 5. (a) CV curves of 500 mM $Ca(BH_4)_2$/THF and 500 mM $Ca(BH_4)_2$/75 mM $Ca(CB_{11}H_{12})_2$/THF electrolytes collected at a scan rate of 10 mV/s. (b) Deposition portion of CV curves in a 500 mM $Ca(BH_4)_2$/THF electrolyte at various scan rates. (c) Deposition portion of CV curves in a 500 mM $Ca(BH_4)_2$/75 mM $Ca(CB_{11}H_{12})_2$/THF electrolyte at various scan rates. The second CV cycle is shown in panels a–c due to alloying/dealloying effects observed in the first CV cycle. (d) Randles–Sevcik plot of the peak deposition current measured in a 500 mM $Ca(BH_4)_2$/75 mM $Ca(CB_{11}H_{12})_2$/THF electrolyte.

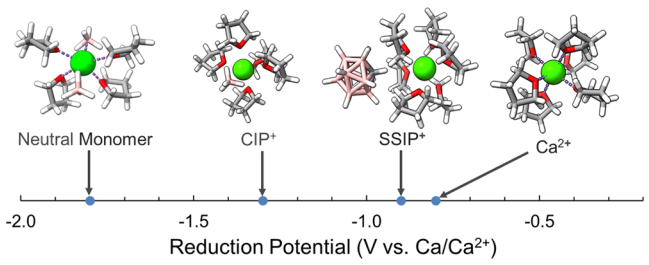

Figure 6. DFT calculations for the standard reduction potential for the first electron transfer to the $Ca(BH_4)_2$ neutral monomer, $CaBH_4^+$ CIP, $Ca(CB_{11}H_{12})^+$ SSIP, and fully solvated Ca^{2+}.

monomers, neutral aggregates (represented as dimers for simplicity), and monovalent ionic species (R2 and R3).[17,27]

$$2Ca(BH_4)_2 \rightleftharpoons Ca_2(BH_4)_4 \quad \text{(R2)}$$

$$Ca_2(BH_4)_4 \rightleftharpoons CaBH_4^+ + Ca(BH_4)_3^- \quad \text{(R3)}$$

The dissociation of the neutral aggregates into ionic species depends in part on the dielectric constant of the electrolyte.[27] The addition of a weakly coordinating salt to a $Ca(BH_4)_2$/THF electrolyte likely alters the dielectric constant of the solution and could drive the formation of additional ionic species from the $Ca(BH_4)_2$ electrolyte without requiring direct interaction between $Ca(BH_4)_2$ and the weakly coordinating salt. Furthermore, weakly coordinating salts in ethereal solvents

https://doi.org/10.1021/acs.jpcc.3c05757
J. Phys. Chem. C 2023, 127, 23664–23674

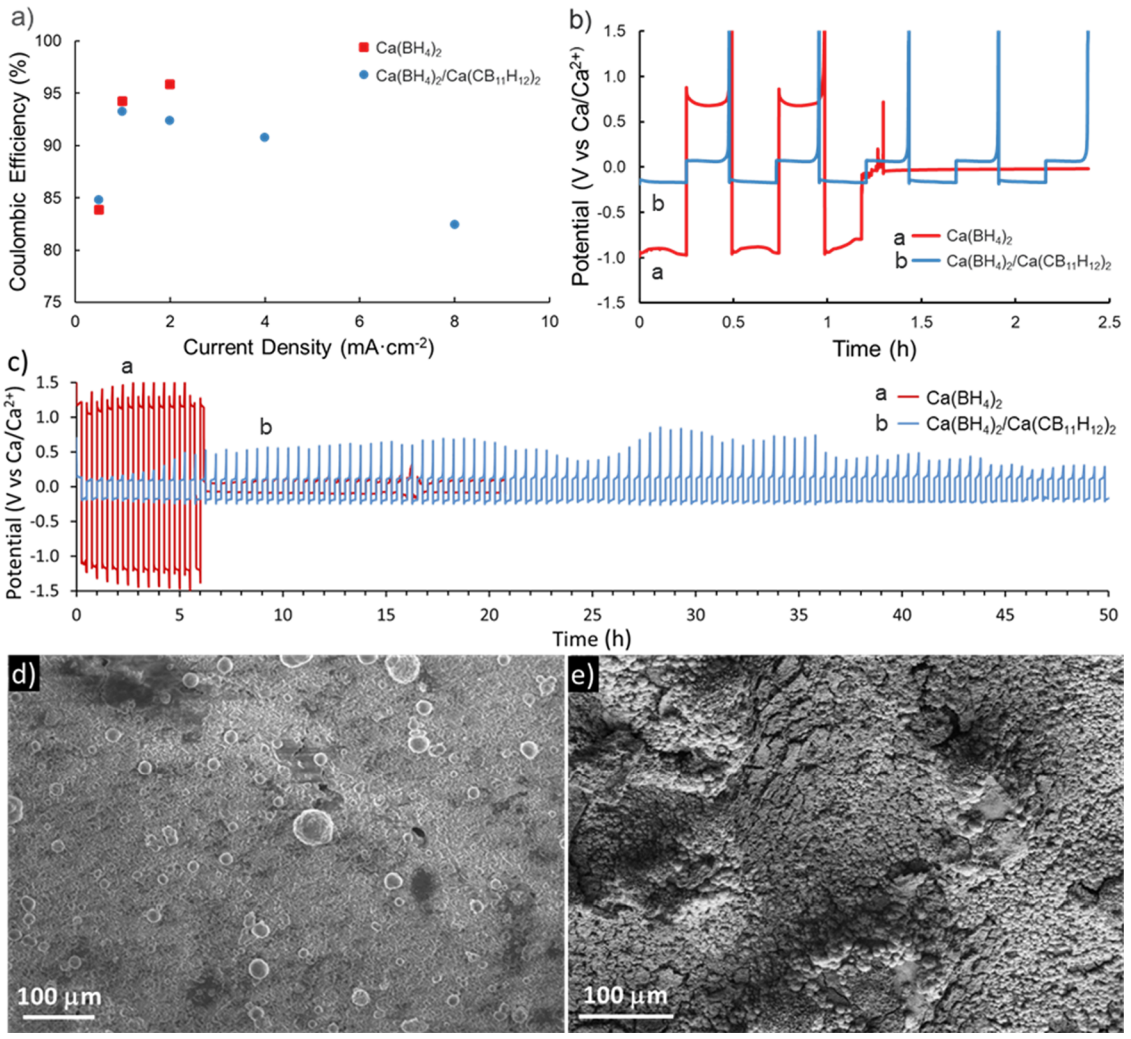

Figure 7. (a) Average Coulombic efficiency for five cycles in a CallAu cell at various current densities and a fixed capacity of 0.5 mAh/cm^2 in 500 mM $Ca(BH_4)_2$/THF and 500 mM $Ca(BH_4)_2$/75 mM $Ca(CB_{11}H_{12})_2$/THF. (b) Example of differences in cycling stability at 2 mA cm^{-2}, with the electrolyte leading to CallAu cell shorting. (c) Extended cycling of 0.5 mAh/cm^2 capacity in a CallCa cell 2 mA/cm^2 rate as a function of electrolyte. (d, e) Resulting morphology produced by extended cycling for 6 h through cell failure (500 mM $Ca(BH_4)_2$/THF) and completing 50 h without cell failure (500 mM $Ca(BH_4)_2$/75 mM $Ca(CB_{11}H_{12})_2$/THF).

can dissociate to produce either the fully solvent-coordinated cation (R4) or SSIPs (R5).[36]

$$Ca(CB_{11}H_{12})_2 \rightleftharpoons Ca^{2+} + 2CB_{11}H_{12}^- \quad \text{(R4)}$$

$$Ca(CB_{11}H_{12})_2 \rightleftharpoons Ca(CB_{11}H_{12})^+_{SSIP} + CB_{11}H_{12}^- \quad \text{(R5)}$$

We assume that the weakly coordinating $CB_{11}H_{12}^-$ has negligible first shell coordination to Ca^{2+}. Additionally, in this mixed-salt electrolyte, ion pairs containing BH_4^- in the first solvation shell and $CB_{11}H_{12}^-$ in the second solvation shell could feasibly form (R6).

$$Ca(BH_4)_2 + Ca(CB_{11}H_{12})^+_{SSIP} \rightleftharpoons CaBH_4^+ + CaBH_4(CB_{11}H_{12})_{SSIP} \quad \text{(R6)}$$

The relative energetics of these potential complexes are unclear a priori. Clearly, understanding the speciation of a $Ca(BH_4)_2$/THF electrolyte as $Ca(CB_{11}H_{12})_2$ is added requires a detailed investigation.

To determine the change in speciation with the added $Ca(CB_{11}H_{12})_2$, we first measure the ionic conductivity of $Ca(BH_4)_2$/$Ca(CB_{11}H_{12})_2$/THF electrolytes (Figure 1). We select 500 mM $Ca(BH_4)_2$ /THF as the base electrolyte because the low conductivity and low concentration of the active $CaBH_4^+$ CIP (~1 mM) at this $Ca(BH_4)_2$ concentration should make changes induced by the added cosalt more readily detectable.[27] As shown in Figure 1a, the addition of $Ca(CB_{11}H_{12})_2$ to the base $Ca(BH_4)_2$ electrolyte yields a significant linear increase in conductivity. This increase is far in excess of that produced by the equivalent addition of $Ca(BH_4)_2$ (Figure 1b). We know that conductivity change with $Ca(BH_4)_2$ addition results from a dipolar neutral aggregate population that drives ionic species generation.[17,27] While the dipolar contributions from these aggregates likely explain the 4−110 mM increase in $Ca(CB_{11}H_{12})_2$ solubility going from THF[26] to the base electrolyte, the abrupt change in conductivity must originate from a more significant change in speciation.

To determine the source of this enhanced conductivity, the direct interaction between $Ca(BH_4)_2$ and $Ca(CB_{11}H_{12})_2$ (R1) is evaluated by probing the borohydride coordination environment. Ca-BH_4 coordination change was monitored using the

https://doi.org/10.1021/acs.jpcc.3c05757
J. Phys. Chem. C 2023, 127, 23664−23674

ν(B−H) spectral region in Raman spectroscopy as a function of added $Ca(CB_{11}H_{12})_2$. As shown in Figure 2a, minimal change in the relative intensities of the BH_4 bands at 2230 and 2324 cm^{-1} occurs with the increased concentration of $Ca(CB_{11}H_{12})_2$. These features were previously shown to be sensitive to the balance of neutral aggregates and charged CIPs,[17] indicating that the BH_4^- coordination environment in this mixed-salt electrolyte strongly resembles that of the base 500 mM $Ca(BH_4)_2$/THF electrolyte, which consists of a mixture of neutral $Ca(BH_4)_2$ and $Ca_2(BH_4)_4$ species. Redistribution of strongly calcium-coordinating BH_4^- to produce cationic $CaBH_4^+$ does not occur with the addition of a weakly coordinated calcium cation to an extent detectable by Raman analysis. The spectroscopic and conductivity data are consistent with the coexistence of two solvation structure populations: one dominated by neutral $Ca(BH_4)_2$ and $Ca_2(BH_4)_4$ species (indicated by Raman spectroscopy) and a second defined by a lack of Ca−BH_4 interactions which is responsible for the enhanced conductivity.

The solvation structure of this second population is difficult to determine by using Raman spectroscopy alone. We can track $CB_{11}H_{12}$ anion addition to the electrolyte using the collective ν(B−H) mode for the cage at 2570 cm^{-1},[44] finding the intensity increasing proportionately with concentration. However, this mode is not expected to differentiate between the second shell and freely solvated anions, as computed differences in frequency are too small for experimental resolution (Figure S1). We experimentally verify this lack of differentiation by comparing the Raman signatures of the free anion, produced with THF solvation of the more weakly coordinating, monovalent trimethylammonium cation ($(CH_3)_3NH^+$) salt, at a concentration equivalent to the added $Ca(CB_{11}H_{12})_2$. No significant difference is observed in the spectral line shape (Figure 2b). This challenge of resolving the second shell and free anion using the Raman analysis has been previously reported for the weakly coordinating TFSI anion.[45] We note that the average THF coordination number will increase with the formation of the SSIP, and this increase should be reflected in the bound THF fraction measured by fitting the ν(C−O)/ν(C−C) Raman spectra (Figure S2).[17] Unfortunately, differentiating between the contribution of increased calcium concentration and increased average solvent coordination number appears infeasible at such a low cosalt concentration. Thus, we must utilize different techniques to determine whether the second population consists of predominantly freely solvated Ca^{2+} or $Ca(CB_{11}H_{12})^+$ SSIPs.

Next, we employed ^{43}Ca NMR to describe the local coordination environment of Ca in these mixed-salt electrolytes. A 500 mM $Ca(BH_4)_2$/THF electrolyte displays a single ^{43}Ca resonance around 20.6 ppm (Figure 3 and Table 1). Addition of $Ca(CB_{11}H_{12})_2$ to this electrolyte induces a linear, upfield chemical shift, indicating a change in the average coordination environment of the calcium ion upon the addition of $Ca(CB_{11}H_{12})_2$. At the saturation concentration of $Ca(CB_{11}H_{12})_2$ (∼110 mM) in 500 mM $Ca(BH_4)_2$/THF, the NMR spectra display a single resonance at 17.5 ppm. Each of the electrolytes produces only a single resonance in the ^{43}Ca NMR spectra, despite the expected presence of multiple Ca species in these electrolytes. We attempted to resolve peaks corresponding to individual Ca species by collecting low-temperature ^{43}Ca NMR spectra of the mixed $Ca(BH_4)_2$/$Ca(CB_{11}H_{12})_2$/THF electrolytes (Figure S3); even at 255 K, we observe only a single ^{43}Ca resonance with relatively little change in the peak position or shape. This observation implies that exchange between the differing Ca solvation environments must be faster than the millisecond timescale employed in NMR. While we are unable to resolve individual peaks for distinct Ca coordination environments, the addition of $Ca(CB_{11}H_{12})_2$ to $Ca(BH_4)_2$/THF electrolytes clearly alters the average coordination environment of calcium.

The speciation changes that drive the ^{43}Ca resonance upfield with $Ca(CB_{11}H_{12})_2$ addition can be described as a shift in the calcium coordination environment from anion (BH_4^-)-dominated interactions to increased solvent (O_{THF}) interactions. We tabulated the chemical shifts from our work and other relevant work in Table 1 along with the validated Ca^{2+} speciation to reveal this trend. First, we examined the chemical shift behavior as a function of the $Ca(BH_4)_2$ concentration without added $Ca(CB_{11}H_{12})_2$. As the concentration of $Ca(BH_4)_2$ increases, the fraction of Ca existing in the neutral dimer and $CaBH_4^+$ CIP structures increases,[27] resulting in a downfield shift of the ^{43}Ca resonance from 20.6 ppm in 0.5 M $Ca(BH_4)_2$/THF to 21.8 ppm in 1.5 M $Ca(BH_4)_2$/THF. These shifts are similar to the previously reported values of 19.1 and 21.4 ppm for 0.5 and 1.5 M $Ca(BH_4)_2$/THF.[46] Interestingly, this work also reports a ^{43}Ca chemical shift of 37.5 ppm for a 0.4 M $Ca(BH_4)_2$/0.4 M $Li(BH_4)_2$/THF electrolyte, which the authors attribute to a structure with lower O coordination of Ca^{2+} in the first solvation shell (Table 1).[46] Consistent with this explanation, a 0.4 M $CaBHFIP_2$/THF electrolyte, containing a mixture of approximately 90% fully solvated Ca^{2+} and 10% $Ca(BHFIP)^+$ SSIP,[36] displays a single ^{43}Ca resonance at −10.0 ppm. Similarly, ^{43}Ca chemical shifts of −19.8 and −19.1 ppm have been reported for 0.1 and 0.5 M $Ca(TFSI)_2$/THF electrolytes, where the first shell coordination of Ca^{2+} is dominated by O coordination from $TFSI^-$ anions and THF molecules.[47] Collectively, these experimental results indicate that the increased coordination of Ca^{2+} by BH_4^- leads to a downfield shift in the ^{43}Ca resonance, while the increased coordination of Ca^{2+} by THF leads to an upfield shift in the ^{43}Ca resonance. Since the mixed $Ca(BH_4)_2$/$Ca(CB_{11}H_{12})_2$/THF electrolytes display an upfield shift relative to the $Ca(BH_4)_2$/THF electrolytes, we conclude that the addition of $Ca(CB_{11}H_{12})_2$ to $Ca(BH_4)_2$/THF electrolytes reduces the average number of BH_4^- in the first solvation shell of Ca^{2+}, consistent with the formation of fully solvated Ca^{2+} (R4), $CaBH_4^+$ (R1), or $Ca(CB_{11}H_{12})^+$ SSIPs (R5).

To determine whether we are producing $Ca(CB_{11}H_{12})^+$ SSIPs, we need to utilize a technique that is sensitive to the production of SSIP structures. We considered X-ray scattering measurements, but ill-defined scattering paths for $CB_{11}H_{12}^-$ second shell occupation, low-scattering cross-section elements that comprise $CB_{11}H_{12}^-$, and the low concentration of the SSIPs would reasonably prevent a definitive coordination signature in an X-ray scattering experiment. Instead, we utilize DRS to measure the change in the solution dielectric constant due to the speciation change of the electrolyte. In particular, the generation of ion pairs produces microwave frequency relaxations which can be utilized to identify the ion pairs.[48,49] Relaxations related to ion pairs typically occur at frequencies lower than relaxations related to the rotation of solvent molecules, enabling the identification of ion pairs within electrolyte solutions.[48] Furthermore, the magnitude of the relaxation is related to the dipole moment of the generated ion pairs according to the Cavell equation.[41] These factors make DRS the ideal tool for detecting the formation of SSIPs due to

https://doi.org/10.1021/acs.jpcc.3c05757
J. Phys. Chem. C 2023, 127, 23664−23674

the large dipole moment generated in these complexes compared to CIPs.[42,48]

Figure 4a presents DRS measurements of mixed $Ca(BH_4)_2$/$Ca(CB_{11}H_{12})_2$/THF electrolytes. As the concentration of $Ca(CB_{11}H_{12})_2$ increases, the real and imaginary components of the dielectric constant also increase, particularly in the lower range of frequencies that we measured. Fitting the DRS measurements enabled the extraction of a total solution dielectric constant (ε_r). Three Debye relaxations were necessary to adequately fit the data for the mixed $Ca(BH_4)_2$/$Ca(CB_{11}H_{12})_2$/THF electrolytes, consistent with the previous DRS analysis of $Ca(BH_4)_2$/THF electrolytes.[27] The fitting parameters are reported in Table S1. The extracted ε_r dramatically increases with the added $Ca(CB_{11}H_{12})_2$, indicating an increase in the number of ion pairs in the mixed-salt electrolyte (Figure 4b).

The slope of ε_r as a function of concentration, also known as the dielectric increment, provides a way to identify the ionic species generated by the addition of $Ca(CB_{11}H_{12})_2$ to $Ca(BH_4)_2$ electrolytes.[27,36] The dielectric increment determined for the mixed-salt electrolyte (70 M^{-1}, Figure 4b) is significantly larger than the previously computed dielectric increments for the $CaBH_4^+$ CIP (20.5 M^{-1}) or the $Ca_2(BH_4)_4$ (16.3 M^{-1}) dimer.[27] The calculated dielectric increments for the $Ca(CB_{11}H_{12})^+$ SSIP (99 M^{-1}) and $CaBH_4(CB_{11}H_{12})$ SSIP (94 M^{-1}) (Figure 4c,d) are closer in magnitude to the experimentally determined values due to the larger dipole moment associated with SSIPs compared to CIPs. This analysis implies that the addition of $Ca(CB_{11}H_{12})_2$ to $Ca(BH_4)_2$ electrolytes primarily generates SSIPs (R5) rather than $CaBH_4^+$ CIPs (R1), as originally hypothesized. While DRS cannot distinguish whether the generated SSIPs contain BH_4^- in the first solvation shell due to the similar dielectric increments for $Ca(CB_{11}H_{12})^+$ SSIP and $CaBH_4(CB_{11}H_{12})$ SSIP, the upfield shift observed in ^{43}Ca NMR suggests a decrease in BH_4^- coordination to Ca^{2+}. Thus, the combination of ^{43}Ca NMR and DRS identify the $Ca(CB_{11}H_{12})^+$ SSIP as a key component of speciation in the mixed $Ca(BH_4)_2$/$Ca(CB_{11}H_{12})_2$/THF electrolytes.

Speciation Controls Deposition. The altered speciation in the mixed $Ca(BH_4)_2$/$Ca(CB_{11}H_{12})_2$/THF electrolyte produces a distinct electrochemical signature compared to that of the $Ca(BH_4)_2$/THF electrolyte. Figure 5a presents the CV curves of $Ca(BH_4)_2$/THF and $Ca(BH_4)_2$/$Ca(CB_{11}H_{12})_2$/THF electrolytes by using Au electrodes at a scan rate of 10 mV/s. Since the $Ca(BH_4)_2$/$Ca(CB_{11}H_{12})_2$/THF electrolyte exhibits a significantly higher conductivity than the $Ca(BH_4)_2$/THF electrolyte, these voltammograms are corrected for R_u arising from the solution resistivity. In both electrolytes, calcium nucleation requires an overpotential of approximately 140 mV at which point calcium deposition begins. However, the shape of the deposition curves differs dramatically. In the 500 mM $Ca(BH_4)_2$/THF electrolyte, the measured current density slowly increases over the applied potential range, with a slightly reduced deposition current observed in the reverse sweep. Clear Ca stripping is observed at potentials positive of 0 V versus Ca/Ca^{2+}. For the 500 mM $Ca(BH_4)_2$/THF electrolyte, the potential appears to briefly become more negative while stripping Ca between +0.05 and +0.10 V versus Ca/Ca^{2+}. This behavior is an artifact of the *iR* correction procedure. In contrast, after Ca nucleates on Au in the 500 mM $Ca(BH_4)_2$/75 mM $Ca(CB_{11}H_{12})_2$/THF electrolyte, the current density increases much more rapidly before peaking around −0.16 V versus Ca/Ca^{2+} and decays in a form reminiscent of a mass-transport-limited electrochemical reaction. The deposition current density in the mixed-salt electrolyte remains significantly greater than that in the $Ca(BH_4)_2$/THF electrolyte. The observed differences in the deposition behavior prompted the investigation of the electrochemical mechanism of deposition through a scan rate-dependent study.

Figure 5b displays the deposition portion of CV curves in the 500 mM $Ca(BH_4)_2$/THF electrolyte (full CV curves can be found as in Figure S4). Critically, variation of the scan rate utilized in CV does not induce a monotonic change in the measured deposition current in the 500 mM $Ca(BH_4)_2$/THF electrolyte, and clear peaks in the deposition current are not observed in the voltammograms. These results imply that calcium deposition from 500 mM $Ca(BH_4)_2$/THF electrolytes, in which $CaBH_4^+$ derived from dimer dissociation (R3) is argued to be the active species, is kinetically limited. Consistent with these results, previous work analyzing CV curves collected using ultramicroelectrodes in 1 M $Ca(BH_4)_2$/THF electrolytes identified a chemical−electrochemical deposition mechanism, with the chemical step being rate-limiting.[18] The reduced current density during the back-sweep of CV also implies mass-transport limitations, indicating that the deposition of calcium from 500 mM $Ca(BH_4)_2$/THF electrolytes requires overcoming both kinetic and mass-transport limitations.

In contrast to the 500 mM $Ca(BH_4)_2$/THF electrolyte, the 500 mM $Ca(BH_4)_2$/75 mM $Ca(CB_{11}H_{12})_2$/THF electrolyte displays mass-transport-limited deposition behavior over a wide range of scan rates (Figure 5c). As the scan rate is increased, the peak current density correspondingly increases linearly with the square root of the scan rate (Figure 5d), indicating a mass-transport-limited mechanism. We calculate a diffusion coefficient of 5.81×10^{-6} cm^2/s for the active Ca^{2+} species from the slope of the Randles−Sevcik equation, which assumes that electron transfer kinetics are fast relative to mass-transport limitations. This value matches well with the D_{BH4} (5.67×10^{-6} cm^2/s) and $D_{CB11H12}$ (5.50×10^{-6} cm^2/s) values that we have determined through PFG−NMR measurements (Figure S5 and Table S3). Because of the increased current density compared to the 500 mM $Ca(BH_4)_2$/THF electrolyte and the Randles−Sevcik-type behavior observed in deposition from the 500 mM $Ca(BH_4)_2$/75 mM $Ca(CB_{11}H_{12})_2$/THF electrolyte but not in the 500 mM $Ca(BH_4)_2$/THF electrolyte, we propose that the reduction of the $Ca(CB_{11}H_{12})^+$ SSIP must be kinetically more facile than the reduction of the $CaBH_4^+$ CIP. In essence, replacing BH_4^- with THF in the first solvation shell of Ca^{2+} improves the electroreduction kinetics while providing a degree of screening by a second shell anion.

In addition to our experimental observations on the kinetics of deposition, the reduction of the $Ca(CB_{11}H_{12})^+$ SSIP is thermodynamically favored over the reduction of the $CaBH_4^+$ CIP. We calculated reduction potentials for the first electron transfer to the neutral $Ca(BH_4)_2$ monomer, the $CaBH_4^+$ CIP, $Ca(CB_{11}H_{12})^+$ SSIP, and fully solvated Ca^{2+} (modeled with an explicit first solvation shell, as shown in Figure 6). Electron transfer to the $Ca(CB_{11}H_{12})^+$ SSIP and fully solvated Ca^{2+} requires the calculated reduction potentials of −0.90 and −0.80 V versus Ca/Ca^{2+}. In contrast, electron transfer to the $Ca(BH_4)_2$ monomer or the $CaBH_4^+$ CIP requires significantly more negative potentials of −1.8 and −1.3 V versus Ca/Ca^{2+}, respectively. These values are relative to the calculated aqueous

https://doi.org/10.1021/acs.jpcc.3c05757
J. Phys. Chem. C 2023, 127, 23664−23674

Ca/Ca^{2+} reduction potential; so, while the trends in these values should be correct, their magnitudes relative to an experimental Ca/Ca^{2+} reference are not necessarily accurate.[50] These calculations demonstrate that having BH_4^- in the first solvation shell of Ca^{2+} induces more negative reduction potentials, consistent with a previous report correlating more strongly bound anions with more negative reduction potentials.[33] By the removal of strongly bound anions from the first solvation shell of Ca, the kinetic and thermodynamic constraints on calcium deposition can be relieved.

To observe the impact of relieved kinetic and thermodynamic constraints on cell performance, we compared the cycling behavior of 500 mM $Ca(BH_4)_2$/THF and 500 mM $Ca(BH_4)_2$/75 mM $Ca(CB_{11}H_{12})_2$/THF electrolytes. We find that these two electrolytes exhibit comparably high (>93%) Coulombic efficiency at a low current density (1 mA/cm^2) for 0.5 mAh/cm^2 capacity in a Ca||Au cell (Figure 7a). The 500 mM $Ca(BH_4)_2$/THF electrolyte exhibits unstable cycling at current densities of 2 mA/cm^2 and above, preventing CE measurement and resulting in cell shorting (Figure 7b), despite the use of a several-millimeter interelectrode gap. We hypothesize that kinetic constraints for the reduction of the $CaBH_4^+$ CIP lead to localized Ca deposition, subsequent dendrite formation, and cell shorting. To test this hypothesis, we transition to a Ca working electrode in a symmetric Ca||Ca cell to determine the electrolyte impact on both cell response and electrode morphology. Stable cycling is sustained for 50 h in the 500 mM $Ca(BH_4)_2$/75 mM $Ca(CB_{11}H_{12})_2$/THF electrolyte, while cell shorting occurs at only 6 h in 500 mM $Ca(BH_4)_2$/THF (Figure 7c). Electron microscopy of the shortened electrode reveals the evidence of localized deposition in the high areal density of Ca nodules distributed across the calcium surface (Figure 7d). Such localized phenomenon and the resulting structure are commonly reported for Ca deposition and cycling.[20,22,26,51] Evidence of localized deposition does not appear on the more extensively cycled electrode in the 500 mM $Ca(BH_4)_2$/75 mM $Ca(CB_{11}H_{12})_2$/THF electrolyte (Figure 7e). The more facile reduction of $Ca(CB_{11}H_{12})^+$ SSIP enables more uniform growth of calcium and cell cycling at current densities of as high as 8 mA cm^{-2}. These results directly link the change in speciation in the mixed-salt electrolyte to a cell-level observable relevant to full calcium battery performance.

CONCLUSIONS

This work provides an example of how altering the speciation of a Ca-ion electrolyte enables the more facile reduction of a calcium coordination complex. In particular, we show that the addition of $Ca(CB_{11}H_{12})_2$ to $Ca(BH_4)_2$/THF produces the $Ca(CB_{11}H_{12})^+$ SSIP as an alternate calcium delivery species. Reduction of calcium from this $Ca(CB_{11}H_{12})^+$ SSIP is more facile kinetically and thermodynamically than the reduction of calcium from the $CaBH_4^+$ CIP. We hypothesize that the SSIP more effectively delivers calcium by providing the electrostatic screening necessary to lower the desolvation barrier and the structural flexibility to allow a close approach to the interface. We propose that facilitating metal deposition through guided SSIP formation is generally applicable to multivalent electrolyte design including Mg-ion and Zn-ion electrolytes. While this work is based on the bulk speciation of electrolytes, we acknowledge that the interfacial speciation may differ. Studies of interfacial speciation through *operando*, surface-sensitive vibrational, and X-ray spectroscopies could further help refine design criteria by providing insights into the location and configuration of the calcium delivery complex. Nevertheless, this work provides insights into designing efficient delivery complexes for Ca-ion electrolytes and demonstrates how mixed-salt electrolytes can provide a design pathway for the creation of Ca^{2+} delivery species.

ASSOCIATED CONTENT

Supporting Information

The Supporting Information is available free of charge at https://pubs.acs.org/doi/10.1021/acs.jpcc.3c05757.

Calculated Raman spectra, Raman determination of coordinated THF, low-temperature ^{43}Ca NMR spectra, additional CV curves, ^{1}H NMR spectra, DRS fitting parameters, additional calculated reduction potentials, diffusion coefficients determined through ^{1}H PFG-NMR, and viscosity measurements (PDF)

AUTHOR INFORMATION

Corresponding Author

Kevin R. Zavadil − *Joint Center for Energy Storage Research, Lemont, Illinois 60439, United States; Material, Physical, and Chemical Sciences Center, Sandia National Laboratories, Albuquerque, New Mexico 87185, United States;* orcid.org/0000-0002-3791-424X; Email: krzavad@sandia.gov

Authors

Alan T. Landers − *Joint Center for Energy Storage Research, Lemont, Illinois 60439, United States; Material, Physical, and Chemical Sciences Center, Sandia National Laboratories, Albuquerque, New Mexico 87185, United States;* orcid.org/0000-0001-7290-711X

Julian Self − *Joint Center for Energy Storage Research, Lemont, Illinois 60439, United States; Energy Technologies Division, Lawrence Berkeley National Laboratory, Berkeley, California 94720, United States; Department of Chemical Engineering, Polytechnique Montreal, Montreal, QC H3T 1J4, Canada;* orcid.org/0000-0002-5486-9559

Scott A. McClary − *Joint Center for Energy Storage Research, Lemont, Illinois 60439, United States; Material, Physical, and Chemical Sciences Center, Sandia National Laboratories, Albuquerque, New Mexico 87185, United States;* orcid.org/0000-0001-9011-1043

Keith J. Fritzsching − *Joint Center for Energy Storage Research, Lemont, Illinois 60439, United States; Material, Physical, and Chemical Sciences Center, Sandia National Laboratories, Albuquerque, New Mexico 87185, United States;* orcid.org/0000-0001-5486-614X

Kristin A. Persson − *Joint Center for Energy Storage Research, Lemont, Illinois 60439, United States; Department of Materials Science and Engineering, UC Berkeley, Berkeley, California 94720, United States; Molecular Foundry, Lawrence Berkeley National Laboratory, Berkeley, California 94720, United States;* orcid.org/0000-0003-2495-5509

Nathan T. Hahn − *Joint Center for Energy Storage Research, Lemont, Illinois 60439, United States; Material, Physical, and Chemical Sciences Center, Sandia National Laboratories, Albuquerque, New Mexico 87185, United States;* orcid.org/0000-0001-6187-4068

Complete contact information is available at: https://pubs.acs.org/10.1021/acs.jpcc.3c05757

Notes

The authors declare no competing financial interest.

■ ACKNOWLEDGMENTS

This work was supported by the Joint Center for Energy Storage Research, an Energy Innovation Hub funded by the U.S. Department of Energy. Sandia National Laboratories is a multimission laboratory managed and operated by National Technology & Engineering Solutions of Sandia, LLC, a wholly owned subsidiary of Honeywell International Inc., for the U.S. Department of Energy's National Nuclear Security Administration under contract DE-NA0003525. This paper describes objective technical results and analyses. Any subjective views or opinions that might be expressed in the paper do not necessarily represent the views of the U.S. Department of Energy or the United States Government.

■ REFERENCES

(1) Trahey, L.; Brushett, F. R.; Balsara, N. P.; Ceder, G.; Cheng, L.; Chiang, Y. M.; Hahn, N. T.; Ingram, B. J.; Minteer, S. D.; Moore, J. S.; et al. Energy storage emerging: A perspective from the Joint Center for Energy Storage Research. *Proc. Natl. Acad. Sci. U.S.A* **2020**, *117* (23), 12550−12557.

(2) Wang, H.; Ryu, J.; Shao, Y.; Murugesan, V.; Persson, K.; Zavadil, K.; Mueller, K. T.; Liu, J. Advancing Electrolyte Solution Chemistry and Interfacial Electrochemistry of Divalent Metal Batteries. *ChemElectroChem.* **2021**, *8* (16), 3013−3029.

(3) Haynes, W. M. *CRC Handbook of Chemistry and Physics*. 97 ed.; CRC Press LLC: 2016; p. 2643.

(4) Hosein, I. D. The Promise of Calcium Batteries: Open Perspectives and Fair Comparisons. *ACS Energy Lett.* **2021**, *6* (4), 1560−1565.

(5) Monti, D.; Ponrouch, A.; Araujo, R. B.; Barde, F.; Johansson, P.; Palacin, M. R. Multivalent Batteries-Prospects for High Energy Density: Ca Batteries. *Front. Chem.* **2019**, *7*, 79.

(6) Kisu, K.; Mohtadi, R.; Orimo, S. I. Calcium Metal Batteries with Long Cycle Life Using a Hydride-Based Electrolyte and Copper Sulfide Electrode. *Adv. Sci.* **2023**, *10* (22), No. e2301178.

(7) Monti, D.; Patil, N.; Black, A. P.; Raptis, D.; Mavrandonakis, A.; Froudakis, G. E.; Yousef, I.; Goujon, N.; Mecerreyes, D.; Marcilla, R.; et al. Polyimides as Promising Cathodes for Metal-Organic Batteries: A Comparison between Divalent (Ca(2+), Mg(2+)) and Monovalent (Li(+), Na(+)) Cations. *ACS Appl. Energy Mater.* **2023**, *6* (13), 7250−7257.

(8) Pavcnik, T.; Forero-Saboya, J. D.; Ponrouch, A.; Robba, A.; Dominko, R.; Bitenc, J. A novel calcium fluorinated alkoxyaluminate salt as a next step towards Ca metal anode rechargeable batteries. *J. Mater. Chem. A* **2023**, *11* (27), 14738−14747.

(9) Chando, P. A.; Chen, S.; Shellhamer, J. M.; Wall, E.; Wang, X.; Schuarca, R.; Smeu, M.; Hosein, I. D. Exploring Calcium Manganese Oxide as a Promising Cathode Material for Calcium-Ion Batteries. *Chem. Mater.* **2023**, *35* (20), 8371−8381.

(10) Smok, T.; Shakouri, S.; Abouzari-Lotf, E.; Pammer, F.; Diemant, T.; Jana, S.; Roy, A.; Xiu, Y.; Klyatskaya, S.; Ruben, M.; et al. A π-Conjugated Porphyrin Complex as Cathode Material Allows Fast and Stable Energy Storage in Calcium Batteries. *Batteries Supercaps* **2023**, No. e202300308, DOI: 10.1002/batt.202300308.

(11) Bier, D.; Li, Z.; Klyatskaya, S.; Sbei, N.; Roy, A.; Riedel, S.; Fichtner, M.; Ruben, M.; Zhao-Karger, Z. Long Cycle-Life Ca Batteries with Poly(anthraquinonylsulfide) Cathodes and Ca-Sn Alloy Anodes. *ChemSusChem* **2023**, *16*, No. e202300932.

(12) Kim, S.; Hahn, N. T.; Fister, T. T.; Leon, N. J.; Lin, X.-M.; Park, H.; Zapol, P.; Lapidus, S. H.; Liao, C.; Vaughey, J. T. Investigation of Rechargeable Calcium Metal-Selenium Batteries Enabled by Borate-Based Electrolytes. *Chem. Mater.* **2023**, *35* (6), 2363−2370.

(13) Blanc, L. E.; Choi, Y.; Shyamsunder, A.; Key, B.; Lapidus, S. H.; Li, C.; Yin, L.; Li, X.; Gwalani, B.; Xiao, Y.; et al. Phase Stability and Kinetics of Topotactic Dual Ca2+−Na+ Ion Electrochemistry in NaSICON NaV2(PO4)3. *Chem. Mater.* **2023**, *35* (2), 468−481.

(14) Ponrouch, A.; Frontera, C.; Barde, F.; Palacin, M. R. Towards a calcium-based rechargeable battery. *Nat. Mater.* **2016**, *15* (2), 169−172.

(15) Biria, S.; Pathreeker, S.; Li, H.; Hosein, I. D. Plating and Stripping of Calcium in an Alkyl Carbonate Electrolyte at Room Temperature. *ACS Appl. Energy Mater.* **2019**, *2* (11), 7738−7743.

(16) Wang, D.; Gao, X.; Chen, Y.; Jin, L.; Kuss, C.; Bruce, P. G. Plating and stripping calcium in an organic electrolyte. *Nat. Mater.* **2018**, *17* (1), 16−20.

(17) Hahn, N. T.; Self, J.; Seguin, T. J.; Driscoll, D. M.; Rodriguez, M. A.; Balasubramanian, M.; Persson, K. A.; Zavadil, K. R. The critical role of configurational flexibility in facilitating reversible reactive metal deposition from borohydride solutions. *J. Mater. Chem. A* **2020**, *8* (15), 7235−7244.

(18) Ta, K.; Zhang, R.; Shin, M.; Rooney, R. T.; Neumann, E. K.; Gewirth, A. A. Understanding Ca Electrodeposition and Speciation Processes in Nonaqueous Electrolytes for Next-Generation Ca-Ion Batteries. *ACS Appl. Mater. Interfaces* **2019**, *11* (24), 21536−21542.

(19) McClary, S. A.; Long, D. M.; Sanz-Matias, A.; Kotula, P. G.; Prendergast, D.; Jungjohann, K. L.; Zavadil, K. R. A Heterogeneous Oxide Enables Reversible Calcium Electrodeposition for a Calcium Battery. *ACS Energy Lett.* **2022**, *7* (8), 2792−2800.

(20) Shyamsunder, A.; Blanc, L. E.; Assoud, A.; Nazar, L. F. Reversible Calcium Plating and Stripping at Room Temperature Using a Borate Salt. *ACS Energy Lett.* **2019**, *4* (9), 2271−2276.

(21) Li, Z.; Fuhr, O.; Fichtner, M.; Zhao-Karger, Z. Towards stable and efficient electrolytes for room-temperature rechargeable calcium batteries. *Energy Environ. Sci.* **2019**, *12* (12), 3496−3501.

(22) Leon, N. J.; Xie, X.; Yang, M.; Driscoll, D. M.; Connell, J. G.; Kim, S.; Seguin, T.; Vaughey, J. T.; Balasubramanian, M.; Persson, K. A.; et al. Room-Temperature Calcium Plating and Stripping Using a Perfluoroalkoxyaluminate Anion Electrolyte. *J. Phys. Chem. C* **2022**, *126* (32), 13579−13584.

(23) Ha, S. Y.; Lee, Y. W.; Woo, S. W.; Koo, B.; Kim, J. S.; Cho, J.; Lee, K. T.; Choi, N. S. Magnesium(II) bis(trifluoromethane sulfonyl) imide-based electrolytes with wide electrochemical windows for rechargeable magnesium batteries. *ACS Appl. Mater. Interfaces* **2014**, *6* (6), 4063−4073.

(24) Ma, Z.; Kar, M.; Xiao, C.; Forsyth, M.; MacFarlane, D. R. Electrochemical cycling of Mg in Mg[TFSI] 2 /tetraglyme electrolytes. *Electrochem. Commun.* **2017**, *78*, 29−32.

(25) Hahn, N. T.; Driscoll, D. M.; Yu, Z.; Sterbinsky, G. E.; Cheng, L.; Balasubramanian, M.; Zavadil, K. R. Influence of Ether Solvent and Anion Coordination on Electrochemical Behavior in Calcium Battery Electrolytes. *ACS Appl. Energy Mater.* **2020**, *3*, 8437−8447.

(26) Kisu, K.; Kim, S.; Shinohara, T.; Zhao, K.; Zuttel, A.; Orimo, S. I. Monocarborane cluster as a stable fluorine-free calcium battery electrolyte. *Sci. Rep.* **2021**, *11* (1), 7563.

(27) Hahn, N. T.; Self, J.; Han, K. S.; Murugesan, V.; Mueller, K. T.; Persson, K. A.; Zavadil, K. R. Quantifying Species Populations in Multivalent Borohydride Electrolytes. *J. Phys. Chem. B* **2021**, *125* (14), 3644−3652.

(28) Sanz-Matias, A.; Roncoroni, F.; Sundararaman, S.; Prendergast, D. Ca-Dimers and Solvent Layering Determine Electrochemically Active Species in $Ca(BH_4)_2$ in THF. *arXiv (Condensed Matter)* **2023**, DOI: 10.1039/c7nr07395j.

(29) Baskin, A.; Lawson, J. W.; Prendergast, D. Anion-Assisted Delivery of Multivalent Cations to Inert Electrodes. *J. Phys. Chem. Lett.* **2021**, *12* (18), 4347−4356.

(30) Holoubek, J.; Baskin, A.; Lawson, J. W.; Khemchandani, H.; Pascal, T. A.; Liu, P.; Chen, Z. Predicting the Ion Desolvation Pathway of Lithium Electrolytes and Their Dependence on Chemistry and Temperature. *J. Phys. Chem. Lett.* **2022**, *13*, 4426−4433, DOI: 10.1021/acs.jpclett.2c00770.

(31) Rajput, N. N.; Qu, X.; Sa, N.; Burrell, A. K.; Persson, K. A. The coupling between stability and ion pair formation in magnesium electrolytes from first-principles quantum mechanics and classical molecular dynamics. *J. Am. Chem. Soc.* **2015**, *137* (9), 3411−3420.
(32) Hahn, N. T.; Seguin, T. J.; Lau, K. C.; Liao, C.; Ingram, B. J.; Persson, K. A.; Zavadil, K. R. Enhanced Stability of the Carba- closo-dodecaborate Anion for High-Voltage Battery Electrolytes through Rational Design. *J. Am. Chem. Soc.* **2018**, *140* (35), 11076−11084.
(33) Connell, J. G.; Zorko, M.; Agarwal, G.; Yang, M.; Liao, C.; Assary, R. S.; Strmcnik, D.; Markovic, N. M. Anion Association Strength as a Unifying Descriptor for the Reversibility of Divalent Metal Deposition in Nonaqueous Electrolytes. *ACS Appl. Mater. Interfaces* **2020**, *12* (32), 36137−36147.
(34) Melemed, A. M.; Skiba, D. A.; Gallant, B. M. Toggling Calcium Plating Activity and Reversibility through Modulation of Ca^{2+} Speciation in Borohydride-Based Electrolytes. *J. Phys. Chem. C* **2022**, *126* (2), 892−902.
(35) Hahn, N. T.; McClary, S. A.; Landers, A. T.; Zavadil, K. R. Efficacy of Stabilizing Calcium Battery Electrolytes through Salt-Directed Coordination Change. *J. Phys. Chem. C* **2022**, *126* (25), 10335−10345.
(36) Hahn, N. T.; Self, J.; Driscoll, D. M.; Dandu, N.; Han, K. S.; Murugesan, V.; Mueller, K. T.; Curtiss, L. A.; Balasubramanian, M.; Persson, K. A.; et al. Concentration-dependent ion correlations impact the electrochemical behavior of calcium battery electrolytes. *Phys. Chem. Chem. Phys.* **2022**, *24*, 674−686.
(37) Frisch, M. J.; Trucks, G. W.; Schlegel, H. B.; Scuseria, G. E.; Robb, M. A.; Cheeseman, J. R.; Scalmani, G.; Barone, V.; Petersson, G. A.; Nakatsuji, H.,et al.*Gaussian 16 Rev. C.01.*; Gaussian, Inc.: Wallingford, CT, 2016.
(38) Chai, J. D.; Head-Gordon, M. Long-range corrected hybrid density functionals with damped atom-atom dispersion corrections. *Phys. Chem. Chem. Phys.* **2008**, *10* (44), 6615−6620.
(39) Tomasi, J.; Mennucci, B.; Cammi, R. Quantum Mechanical Continuum Solvation Models. *Chem. Rev.* **2005**, *105*, 2999−3093.
(40) Cancès, E.; Mennucci, B.; Tomasi, J. A new integral equation formalism for the polarizable continuum model: Theoretical background and applications to isotropic and anisotropic dielectrics. *J. Chem. Phys.* **1997**, *107* (8), 3032−3041.
(41) Cavell, E. A. S.; Knight, P. C.; Sheikh, M. A. Dielectric Relaxation in Non Aqueous Solutions. Part 2. - Solutions of tri(n-butyl)ammonium picrate and iodide in polar solvents. *Trans. Faraday Soc.* **1971**, *67*, 2225−2233.
(42) Sonnleitner, T.; Nikitina, V.; Nazet, A.; Buchner, R. Do H-bonds explain strong ion aggregation in ethylammonium nitrate + acetonitrile mixtures? *Phys. Chem. Chem. Phys.* **2013**, *15* (42), 18445−18452.
(43) Hou, S.; Ji, X.; Gaskell, K.; Wang, P.-F.; Wang, L.; Xu, J.; Sun, R.; Borodin, O.; Wang, C. Solvation sheath reorganization enables divalent metal batteries with fast interfacial charge transfer kinetics. *Science* **2021**, *374*, 172−178.
(44) Kononova, E. G.; Bukalov, S. S.; Leites, L. A.; Lyssenko, K. A.; Ol'shevskaya, V. A. Vibrational spectra and structure of cesium salts of icosahedral monocarba-*closo*-dodecaborate anion, $[CB_{11}H_{12}]^-$ and its *nido*- derivative, $[CB_{10}H_{13}]^-$. *Russ. Chem. Bull., Int. Ed.* **2003**, *52* (1), 85−92.
(45) Henderson, W. A.; Seo, D. M.; Han, S.-D.; Borodin, O. Electrolyte Solvation and Ionic Association. VII. Correlating Raman Spectroscopic Data with Solvate Species. *J. Electrochem. Soc.* **2020**, *167*, 110551.
(46) Jie, Y.; Tan, Y.; Li, L.; Han, Y.; Xu, S.; Zhao, Z.; Cao, R.; Ren, X.; Huang, F.; Lei, Z.; et al. Electrolyte Solvation Manipulation Enables Unprecedented Room-Temperature Calcium-Metal Batteries. *Angew. Chem., Int. Ed.* **2020**, *59* (31), 12689−12693.
(47) Hu, J. Z.; Jaegers, N. R.; Hahn, N. T.; Hu, W.; Han, K. S.; Chen, Y.; Sears, J. A.; Murugesan, V.; Zavadil, K. R.; Mueller, K. T. Understanding the Solvation-Dependent Properties of Cyclic Ether Multivalent Electrolytes Using High-Field NMR and Quantum Chemistry. *JACS Au* **2022**, *2* (4), 917−932.
(48) Buchner, R.; Hefter, G. Interactions and dynamics in electrolyte solutions by dielectric spectroscopy. *Phys. Chem. Chem. Phys.* **2009**, *11* (40), 8984−8999.
(49) Buchner, R. What can be learnt from dielectric relaxation spectroscopy about ion solvation and association? *Pure Appl. Chem.* **2008**, *80* (6), 1239−1252.
(50) Araujo, R. B.; Thangavel, V.; Johansson, P. Towards novel calcium battery electrolytes by efficient computational screening. *Energy Storage Mater.* **2021**, *39*, 89−95.
(51) Pavcnik, T.; Lozinsek, M.; Pirnat, K.; Vizintin, A.; Mandai, T.; Aurbach, D.; Dominko, R.; Bitenc, J. On the Practical Applications of the Magnesium Fluorinated Alkoxyaluminate Electrolyte in Mg Battery Cells. *ACS Appl. Mater. Interfaces* **2022**, *14*, 26766.

https://doi.org/10.1021/acs.jpcc.3c05757
J. Phys. Chem. C 2023, 127, 23664−23674